Supporting Information for Spin Wave Radiation by a Topological Charge Dipole

Sebastián A. Díaz,[*,†] Tomoki Hirosawa,[‡] Daniel Loss,[†] and Christina Psaroudaki[*,¶,§]

†*Department of Physics, University of Basel, Klingelbergstrasse 82, CH-4056 Basel, Switzerland*

‡*Department of Physics, University of Tokyo, Bunkyo, Tokyo 113-0033, Japan*

¶*Department of Physics, California Institute of Technology, Pasadena, CA 91125, USA*

§*Institute for Theoretical Physics, University of Cologne, D-50937 Cologne, Germany*

E-mail: s.diaz@unibas.ch; cpsaroud@caltech.edu

Supplementary Note 1: Micromagnetic Simulations

We consider the following spin-lattice Hamiltonian, defined on a 2D lattice structure,

$$H = -\tfrac{1}{2}\sum_{\mathbf{r},i}(J\mathbf{S}_{\mathbf{r}}\cdot\mathbf{S}_{\mathbf{r}\pm a\mathbf{e}_i} + D\mathbf{d}_{\pm\mathbf{e}_i}\cdot\mathbf{S}_{\mathbf{r}}\times\mathbf{S}_{\mathbf{r}\pm a\mathbf{e}_i}) + H_z\,, \tag{S1}$$

where $\mathbf{S}_{\mathbf{r}}$ is a spin-S operator at site $\mathbf{r}$, and $H_z = -\sum_{\mathbf{r}} g\mu_B B S^z_{\mathbf{r}}$ is the Zeeman energy along the z axis. J and D represent the exchange and DM[1,2] couplings respectively, g is the g-factor, μ_B the Bohr magneton, a is the lattice constant, and $\mathbf{e}_{x,y}$ are the unit vectors in the x and y directions respectively. The DM interaction, which satisfies $\mathbf{d}_{\mathbf{e}_i} = -\mathbf{d}_{-\mathbf{e}_i}$, is the

result of spin-orbit coupling and lack of inversion symmetry, and is dictated by the crystal symmetry of a given material.

To simulate the magnetization dynamics of the insulating bilayer, we numerically solve the Landau-Lifshitz-Gilbert (LLG) equation,[3]

$$\frac{d\mathbf{n}_{\mathbf{r}}^{i}}{dt} = -\frac{\gamma_0 \mathbf{n}_{\mathbf{r}}^{i}}{1+\alpha^2} \times \left(\mathbf{H}_{\text{eff}} + \alpha \mathbf{n}_{\mathbf{r}}^{i} \times \mathbf{H}_{\text{eff}}\right) , \tag{S2}$$

where $\mathbf{H}_{\text{eff}} = -(1/\gamma_0\hbar)\partial H/\partial \mathbf{n}_{\mathbf{r}}^{i}$, for each of the $i = 1, 2$ layers. We consider two coupled monolayers of a finite lattice of 180×120 sites in the xy plane. Here $\mathbf{n}_{\mathbf{r}}^{i} = \mathbf{S}_{\mathbf{r}}^{i}/M_s$ with $M_s = g\mu_B S/a^2 d$ the saturation magnetization, γ_0 is the gyromagnetic ratio, α is the Gilbert damping coefficient describing spin relaxation, and d the layer thickness. Time t, frequency ω, and space $\mathbf{r}$ are given in dimensionless units. Physical units are restored as $\tilde{t} = \hbar t/JS$, $\tilde{\mathbf{r}} = \mathbf{r}a$, and $\tilde{\omega} = JS\omega/\hbar$. H is the total Hamiltonian including an external time-oscillating magnetic field along the x axis, $H = H_T + H_{\text{osc}}$, with $H_T = H_1 + H_2 + H_{\text{int}}$ and $H_{\text{osc}} = -\sum_{\mathbf{r}} g\mu_B B_0 \cos(\omega t)(n_{\mathbf{r}}^{x,1} + n_{\mathbf{r}}^{x,2})$. The simulations were performed using $J = 1$, $\alpha = 0.08$, $b_0 = g\mu_B B_0/JS = 0.1$, and unless explicitly stated, $D = 1$. The value of the uniform field ranges between $0.6 \leq b \leq 0.9$, of the interlayer coupling between $0 \leq J_{\text{int}} \leq 0.3$, of the external frequency between $0.6 \leq \omega \leq 0.85$. The initial spin configurations supported by the Hamiltonian Eq. (S1), before the onset of the oscillating field, correspond to spin textures carrying a finite Q and are calculated by means of a Monte Carlo simulated annealing method. They correspond to initial states for the simulation of the time-evolution of magnetic moments of Eq. (S2). We numerically verify that a time-oscillating field along the x direction activates the CCW mode for a skyrmion and the CW mode for an antiskyrmion, signaled by a resonance peak at $\omega \simeq b$. In order to minimize finite size effects for the results of the section Dispersion Characterization, we consider a larger lattice of $N_x \times N_y$ sites in the xy plane, with $N_x = 360$ and $N_y = 120$.

Supplementary Note 2: Skyrmion/Antiskyrmion Center of Mass

The collective coordinate of position R_i^ν, for a spin field $\mathbf{n}_\mathbf{r}^i$ defined on a discrete square lattice, is given by

$$R_i^\nu = \frac{1}{Q_i}\sum_{\mathbf{r}}(\mathbf{r}\cdot\mathbf{e}_\nu + \tfrac{1}{2}a)\sigma_\mathbf{r}^i\,. \tag{S3}$$

Here

$$\sigma_\mathbf{r}^i = (\Omega^i_{\mathbf{r},\mathbf{r}+a\mathbf{e}_x,\mathbf{r}+a\mathbf{e}_x+a\mathbf{e}_y} + \Omega^i_{\mathbf{r},\mathbf{r}+a\mathbf{e}_x+a\mathbf{e}_y,\mathbf{r}+a\mathbf{e}_y})/4\pi \tag{S4}$$

is the discretized topological charge[4] over a square plaquette centered at $\mathbf{r}+\frac{1}{2}a(\mathbf{e}_x+\mathbf{e}_y)$, computed in terms of the solid angles subtended by the spins at sites $\{\mathbf{r},\mathbf{r}+a\mathbf{e}_x,\mathbf{r}+a\mathbf{e}_x+a\mathbf{e}_y\}$ and $\{\mathbf{r},\mathbf{r}+a\mathbf{e}_x+a\mathbf{e}_y,\mathbf{r}+a\mathbf{e}_y\}$ using the expression[5]

$$\tan\left[\tfrac{1}{2}\Omega^i_{\mathbf{r}_1,\mathbf{r}_2,\mathbf{r}_3}\right] = \frac{\mathbf{n}^i_{\mathbf{r}_1}\cdot\mathbf{n}^i_{\mathbf{r}_2}\times\mathbf{n}^i_{\mathbf{r}_3}}{1+\mathbf{n}^i_{\mathbf{r}_1}\cdot\mathbf{n}^i_{\mathbf{r}_2}+\mathbf{n}^i_{\mathbf{r}_1}\cdot\mathbf{n}^i_{\mathbf{r}_3}+\mathbf{n}^i_{\mathbf{r}_2}\cdot\mathbf{n}^i_{\mathbf{r}_3}}\,. \tag{S5}$$

Finally, $Q_i=\sum_\mathbf{r}\sigma_\mathbf{r}^i$ is the topological charge of $\mathbf{n}_\mathbf{r}^i$ over the entire lattice.

Supplementary Note 3: Fourier Transform Radiation Pattern

In order to reveal the radiation pattern of the emitted spin waves we used $\delta n^z_\mathbf{k}$, the absolute value of the Fourier Transform of $\delta n^z_\mathbf{r}(t) = n^z_\mathbf{r}(t) - n^z_{\mathrm{FM}}(t)$, averaged over one period of the ac driving field. To further enhance the far-field spin wave amplitude features, the sign of the Hilbert Transform Filter of $\delta n^z_\mathbf{r}(t)$ was obtained before taking the Fourier Transform. The Hilbert Transform Filter enhances the maxima and minima of the z component of the magnetization field, thus making it easier to extract the spatial periodicities using the Fourier

Transform. The full expression is given below

$$\delta n^z_{\mathbf{k}} = \frac{1}{T}\int_0^T dt\, |\mathcal{F}_{\mathbf{k}}[\mathrm{sign}(\mathcal{H}[\delta n^z_{\mathbf{r}}(t)])]| \ . \tag{S6}$$

Supplementary Note 4: Spin Wave Characteristics

In this Supplementary Note we provide further details on the characteristics of the emitted SWs. For Type III bilayers, SWs have a spiral structure with a preferred sense of rotation determined by the sign of the topological charge of the source, as is illustrated in Fig. S1. For two layers hosting skyrmions (antiskyrmions) with $Q = -1$ ($Q = 1$), the charge separation distance $\mathbf{R}_0$, which plays the role of the source, performs a CCW (CW) rotation, and the emitted SWs have a spiral (antispiral) shape. To verify whether the spiral SWs are emitted

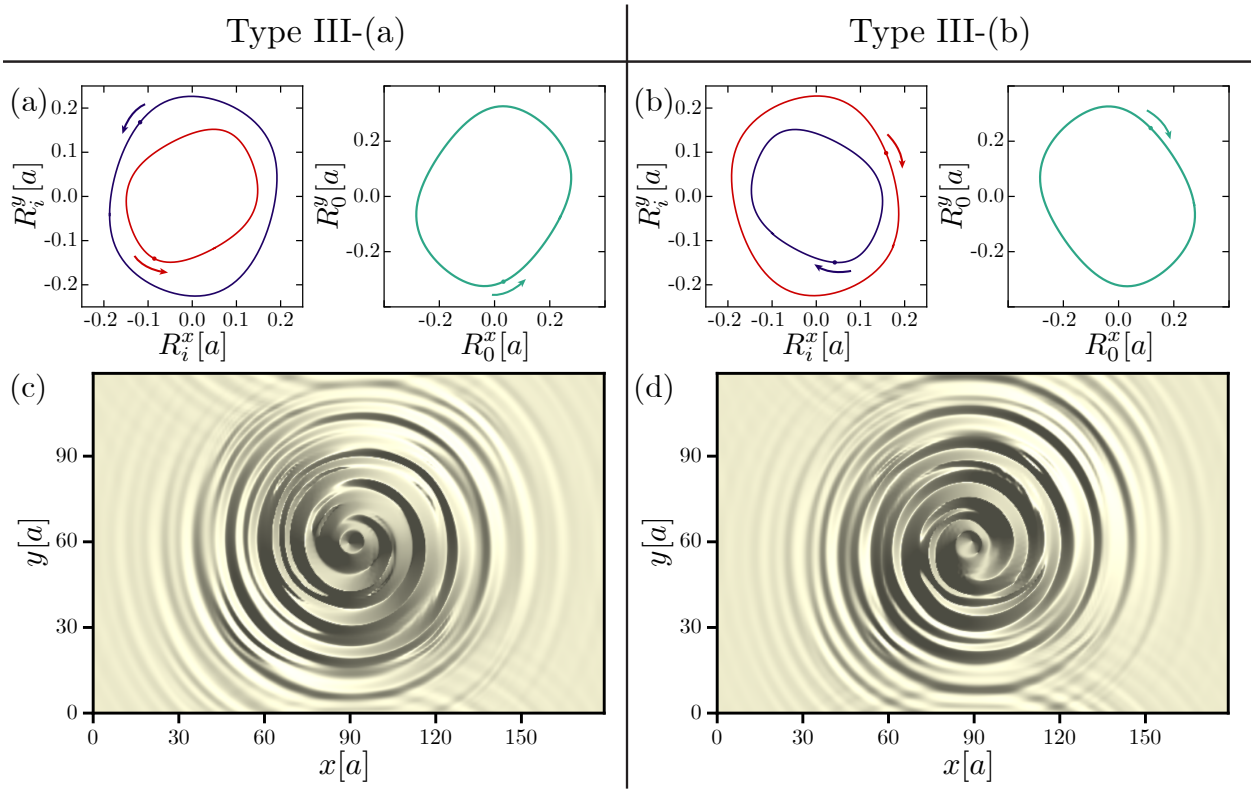

Figure S1: Spirals and Antispirals. The direction of spiral rotation depends on the topological charge Q. (a) The charge seperation distance $\mathbf{R}_0$ rotates in a CCW manner in Type III-(a) bilayers, (b) and in a CW manner in Type III-(b) bilayers. (c) The direction of the spiral SW of Type III-(a) is opposite compared to (d) antispirals of of Type III-(b).

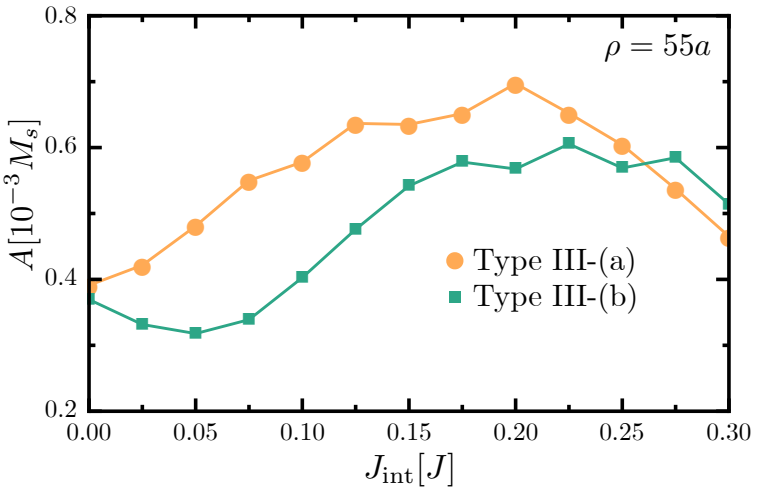

Figure S2: Far-field amplitude A as a function of interlayer coupling $J_{\rm int}$ for Type III, $\rho = 55a$, and $b = 0.6 = \omega$. A shows an irregular behavior on $J_{\rm int}$, that could be the result of interference patterns, or an unsuitable choice of an annulus area $\mathcal{J}$ for the analysis of the emitted SWs with a spiral structure.

by a source consisting of two interacting particles, in Fig. S2 we plot the far-field amplitude A as a function of the interlayer coupling $J_{\rm int}$, for $\rho = 55a$. For Type III-(a), A is an increasing function for $J_{\rm int} < 0.2$, while it decreases for $J_{\rm int} \geq 0.2$. On the contrary, for Type III-(b) A has a small decrease for small $J_{\rm int}$ and later increases at a slow rate. This irregular behavior on $J_{\rm int}$ could be the result of interference patterns, or unsuitable choice of an annulus area $\mathcal{J}$ for the analysis of emitted SWs with a spiral structure. To obtain conclusive results, a systematic way to exclude interference patterns, as well as the consideration of different geometries $\mathcal{J}$, need to be employed.

An additional mechanism to tune the far-field amplitude A is by varying the external out-of-plane magnetic field b. In Fig. S3, we plot A as a function of b for $J/D = 1$, $J_{\rm int} = 0.3J$, and $\rho = 55a$. As expected, A is decreased fast by increasing b for both Type I and II. For large magnetic fields $b \gtrsim 0.7$ the spins tend to align along the direction of the field, and local perturbations of the z-component vanish. We emphasize that no variation in the value of A appears between the various subtypes of Type I and II bilayer. A small difference of the value of A between Type I-(a)-(b) and Type I-(c)-(d) (green line) is reported in the inset of Fig. S3, when measured closer to the source for $\rho = 30a$.

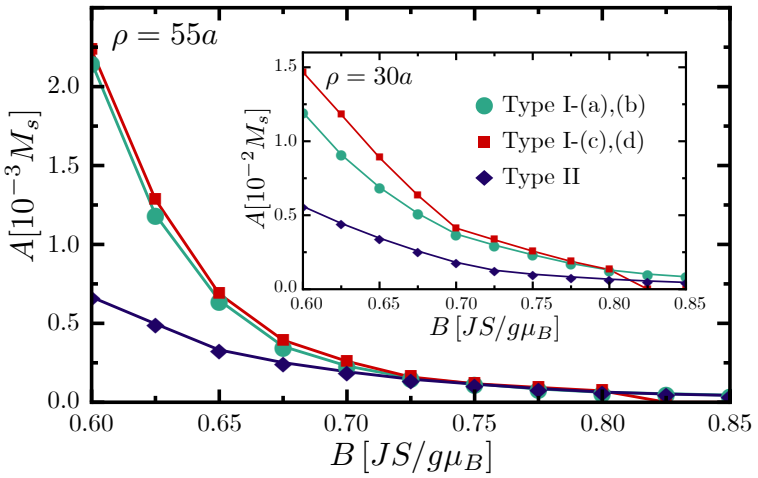

Figure S3: Far-field amplitude A as a function of external out-of-plane magnetic field b for $\rho = 55a$, $J_{\text{int}} = 0.3J$, and on-resonance frequency $\omega = b$. A decreases fast with b for both Type I (red line) and II (blue line) bilayers, indicating that for large magnetic fields, local perturbations of the z-component vanish. The inset reports a small difference of the value of A between Type I-(a)-(b) (green line) and Type I-(c)-(d) (red line) for $\rho = 30a$ closer to the source.

Finally, in Fig. S4 we demonstrate how the relative helicity $\tilde{\gamma}$ of the charge dipole for Type I bilayers can be used to manipulate the propagation direction of the spin waves in the 2D plane. Our results suggest that in Type I bilayers, the charge separation distance performs a time-periodic motion on a straight path obtained by rotating the x axis by an angle $\psi = \tan^{-1}[\sin(\tilde{\gamma})]$, which coincides with the emission direction of SWs. A Type I-(a) bilayer emits waves in the $\psi = \pi/4$ direction, a Type I-(b) in the $\psi = -\pi/4$, and the Types I-(c) and (d) in the $\psi = 0$ direction, as illustrated in Fig. S4.

Supplementary Note 5: Spin Wave Hamiltonian

In the main text we argued that the sense of gyration of localized deformations of the magnetization profile depends on the sign of Q, which we now substantiate by a numerical calculation of the magnon spectrum for all types of magnetic textures studied here. We consider the spin-lattice Hamiltonian of Eq. (1) from the main text with $\{\mathbf{d}_{\mathbf{e}_x}, \mathbf{d}_{\mathbf{e}_y}\} = \{-\mathbf{e}_x, -\mathbf{e}_y\}$ for cubic, $\{\mathbf{d}_{\mathbf{e}_x}, \mathbf{d}_{\mathbf{e}_y}\} = \{-\mathbf{e}_y, \mathbf{e}_x\}$ for interfacial, $\{\mathbf{d}_{\mathbf{e}_x}, \mathbf{d}_{\mathbf{e}_y}\} = \{\mathbf{e}_y, \mathbf{e}_x\}$ for C_{2v},

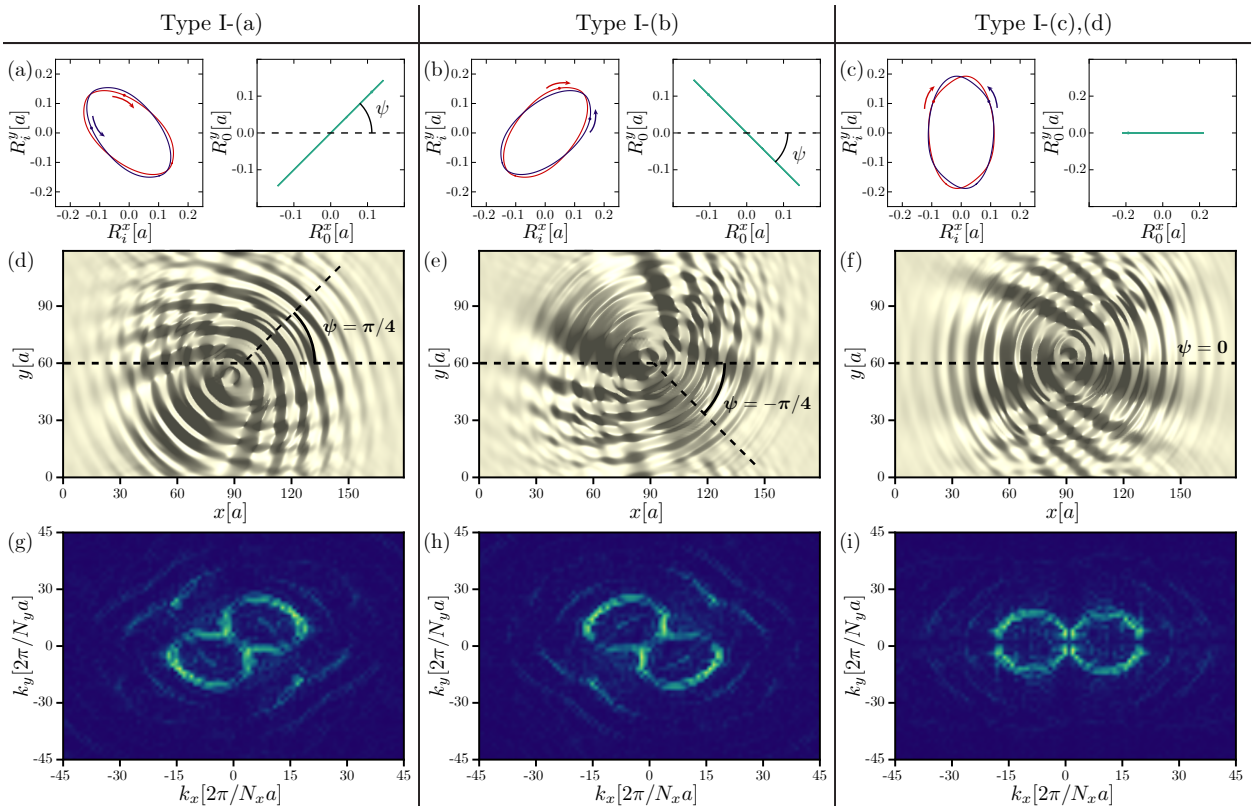

Figure S4: Relation between the dynamics of the collective coordinate of position $\mathbf{R}_i(t)$ and the preferred directionality of the radiated SWs for Type I bilayer that corresponds to the topological charge dipole. In all cases we use $J/D = 1$, $b = 0.6$ ($B = 0.6JS/g\mu_B$), and $\omega = 0.6$ ($\tilde{\omega} = 0.6JS/\hbar$). (a)-(c) Blue lines denote the path of $\mathbf{R}_i$ for the texture in layer 1, red lines for the one in layer 2, while arrows indicate the sense of gyration. The green lines denote the path of the charge separation distance $\mathbf{R}_0 = \mathbf{R}_1 - \mathbf{R}_2$. (d)-(f) Snapshots of the perpendicular magnetization deviation $\delta n^z_{\mathbf{r}}(t)$, and (g)-(i) the radiation pattern $\delta n^z_{\mathbf{k}}$. SWs are radiated by a spin-wave antenna with a preferred direction with respect to x axis, $\psi = \tan^{-1}[\sin(\tilde{\gamma})]$, determined by the helicity of the emitter $\tilde{\gamma} = \gamma_1 - \gamma_2$. We find $\psi = \pi/4$ for Type I-(a), $\psi = -\pi/4$ for Type I-(b), and $\psi = 0$ for Type I-(c), (d).

and $\{\mathbf{d}_{\mathbf{e}_x}, \mathbf{d}_{\mathbf{e}_y}\} = \{\mathbf{e}_x, -\mathbf{e}_y\}$ for D_{2d} crystal symmetry. Quantum spin fluctuations are described using Holstein-Primakoff (HP) bosons. In the case of noncollinear textures, such as those investigated here, it is necessary to first choose the spin quantization axis along the direction of the classical ground state $\mathbf{n}_{\mathbf{r}}$. This is accomplished by introducing an orthonormal basis at each lattice site, $\{\mathbf{m}^1_{\mathbf{r}}, \mathbf{m}^2_{\mathbf{r}}, \mathbf{n}_{\mathbf{r}}\}$, with $\mathbf{m}^1_{\mathbf{r}} \times \mathbf{m}^2_{\mathbf{r}} = \mathbf{n}_{\mathbf{r}}$. We can now introduce the rotated spin operators at each site according to $\mathbf{S}_{\mathbf{r}} = \mathbf{m}^1_{\mathbf{r}}\mathsf{S}^1_{\mathbf{r}} + \mathbf{m}^2_{\mathbf{r}}\mathsf{S}^2_{\mathbf{r}} + \mathbf{n}_{\mathbf{r}}\mathsf{S}^3_{\mathbf{r}}$. The HP

transformation at site $\mathbf{r}$ then reads

$$\mathsf{S}^{+}_{\mathbf{r}} = (2S - a^{\dagger}_{\mathbf{r}} a_{\mathbf{r}})^{1/2} a_{\mathbf{r}} \,, \tag{S7}$$

$$\mathsf{S}^{-}_{\mathbf{r}} = a^{\dagger}_{\mathbf{r}} (2S - a^{\dagger}_{\mathbf{r}} a_{\mathbf{r}})^{1/2} \,, \tag{S8}$$

$$\mathsf{S}^{3}_{\mathbf{r}} = S - a^{\dagger}_{\mathbf{r}} a_{\mathbf{r}} \,, \tag{S9}$$

where $\mathsf{S}^{\pm}_{\mathbf{r}} = \mathsf{S}^{1}_{\mathbf{r}} \pm i\mathsf{S}^{2}_{\mathbf{r}}$, and with the HP boson operators satisfying the bosonic algebra: $[a_{\mathbf{r}}, a^{\dagger}_{\mathbf{r}'}] = \delta_{\mathbf{r},\mathbf{r}'}$ and $[a_{\mathbf{r}}, a_{\mathbf{r}'}] = 0 = [a^{\dagger}_{\mathbf{r}}, a^{\dagger}_{\mathbf{r}'}]$. Following a standard procedure, the spin-lattice Hamiltonian is expanded as a series in $1/S$. The spin wave Hamiltonian, identified as the $\mathcal{O}(S)$ piece, has the form

$$H_{\rm SW} = \tfrac{1}{2} S \sum_{\mathbf{r},\mathbf{r}'} \mathcal{X}^{\dagger}_{\mathbf{r}} \begin{pmatrix} \Omega_{\mathbf{r},\mathbf{r}'} & -\Delta_{\mathbf{r},\mathbf{r}'} \\ -\Delta^{*}_{\mathbf{r},\mathbf{r}'} & \Omega^{*}_{\mathbf{r},\mathbf{r}'} \end{pmatrix} \mathcal{X}_{\mathbf{r}'} - \tfrac{1}{2} S \sum_{\mathbf{r}} \Lambda_{\mathbf{r}} \,, \tag{S10}$$

where $\mathcal{X}^{\dagger}_{\mathbf{r}} = \left(a^{\dagger}_{\mathbf{r}} \,,\, a_{\mathbf{r}} \right)$, $\Lambda_{\mathbf{r}} = \sum_{\mathbf{r}'} \left[J_{\mathbf{r},\mathbf{r}'} \left(\mathbf{n}_{\mathbf{r}} \cdot \mathbf{n}_{\mathbf{r}'} \right) + \boldsymbol{D}_{\mathbf{r},\mathbf{r}'} \cdot \left(\mathbf{n}_{\mathbf{r}} \times \mathbf{n}_{\mathbf{r}'} \right) \right] + \frac{g\mu_B B}{S} n^{z}_{\mathbf{r}}$, $\Omega_{\mathbf{r},\mathbf{r}'} = \delta_{\mathbf{r},\mathbf{r}'} \Lambda_{\mathbf{r}} - \frac{1}{2} \left[J_{\mathbf{r},\mathbf{r}'} (\mathbf{m}^{+}_{\mathbf{r}} \cdot \mathbf{m}^{-}_{\mathbf{r}'}) + \boldsymbol{D}_{\mathbf{r},\mathbf{r}'} \cdot (\mathbf{m}^{+}_{\mathbf{r}} \times \mathbf{m}^{-}_{\mathbf{r}'}) \right]$, $\Delta_{\mathbf{r},\mathbf{r}'} = \frac{1}{2} \left[J_{\mathbf{r},\mathbf{r}'} (\mathbf{m}^{+}_{\mathbf{r}} \cdot \mathbf{m}^{+}_{\mathbf{r}'}) + \boldsymbol{D}_{\mathbf{r},\mathbf{r}'} \cdot (\mathbf{m}^{+}_{\mathbf{r}} \times \mathbf{m}^{+}_{\mathbf{r}'}) \right]$, with $J_{\mathbf{r},\mathbf{r}'} = J(\delta_{\mathbf{r}-\mathbf{r}',\pm a\mathbf{e}_x} + \delta_{\mathbf{r}-\mathbf{r}',\pm a\mathbf{e}_y})$, $\boldsymbol{D}_{\mathbf{r},\mathbf{r}'} = D(\mathbf{d}_{\pm\mathbf{e}_x} \delta_{\mathbf{r}-\mathbf{r}',\pm a\mathbf{e}_x} + \mathbf{d}_{\pm\mathbf{e}_y} \delta_{\mathbf{r}-\mathbf{r}',\pm a\mathbf{e}_y})$, and $\mathbf{m}^{\pm}_{\mathbf{r}} = \mathbf{m}^{1}_{\mathbf{r}} \pm i\mathbf{m}^{2}_{\mathbf{r}}$.

In the following we discuss the spectrum and form of excitations around the equilibrium magnetization profile, which can be either a skyrmion or an antiskyrmion, obtained by a numerical diagonalization of Eq. (S10), performed for $J/D = 1$ on a square of 30×30 spins with periodic boundary conditions. In Fig. S5, we depict the energies of the 10 lowest-lying magnon modes as a function of the external magnetic field. First we note that the magnon spectrum is insensitive to the choice of Q and γ; any combination of topological charge and helicity reproduces the same energy spectrum. We observe however, that the sense of gyration of localized deformations of the magnetization profile depends on the sign of Q. Local modes of the skyrmion with a CCW sense of gyration, correspond to CW modes for the antiskyrmion. This observation is confirmed by an analytical derivation of the magnon

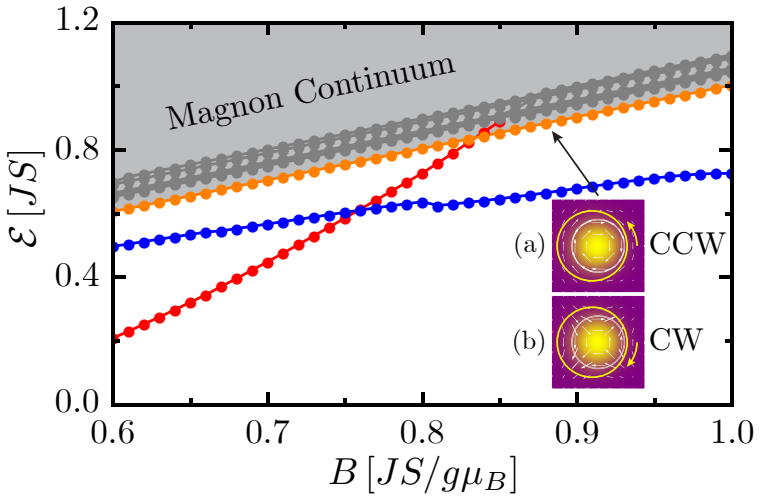

Figure S5: Magnetic field dependence of the magnon energy $\mathcal{E}$, derived by a numerical diagonalization of the spin wave Hamiltonian (S10), for $J/D = 1$, on a square of 30×30 spins, in the presence of a single skyrmion with $\gamma = -\pi/2$ and $Q = -1$. In addition to the magnon continuum (shaded region) with a boundary $\varepsilon_{\rm gap} = b$, we find a breathing (blue line), an elliptical (red line), and a counter-clockwise (CCW) localized mode (orange line), visualized in inset (a). The magnon energy is independent of the choice of γ and Q, but the sense of gyration for the corresponding eigenstates depends on the sign of Q. Thus, the orange line corresponds a clockwise (CW) mode for an antiskyrmion, visualized in inset (b).

eigenvalue problem derived in the continuum model, given explicitly in Supplementary Note 6.

Several important facts have become apparent in Fig. S5, which we analyze. The grey shaded area represents the magnon continuum which exists above the gap due to the magnetic field $\varepsilon_{\rm gap} = g\mu_B B$. Below the gap of the scattering states, we find three bound states, two of them correspond to the breathing mode (blue line) and the elliptical (red line). Of particular importance for the present study is the localized state with energy just below the magnon gap (orange line), $\mathcal{E}_0 \approx \varepsilon_{\rm gap}$, which corresponds to the counterclockwise (CCW) mode for the skyrmion, and as already suggested, to the clockwise (CW) mode for the antiskyrmion. These modes correspond to a rotation of the out-of-plane spin components around the (anti)skyrmion core. The CCW and CW modes are excited by an in-plane ac magnetic field, while exciting the breathing mode requires an out-of-plane ac magnetic field. Finally, a zero energy mode is found, associated with translations of the skyrmion position

in the 2D plane (not shown).

Supplementary Note 6: Continuum limit

Here we present the continuum model of the discrete magnetic Hamiltonian of Eq. (1) from the main text, the corresponding stable solutions and the structure of the magnon eigenvalue problem, in order to demonstrate that the sense of gyration of localized deformations of the magnetization profile depends on the topological charge Q. To derive the classical energy functional in the continuum, valid in the limit of slowly varying magnetic textures, we treat the spin operators as classical vectors of length S, $\mathbf{S_r} \to S\mathbf{n_r}$, where $\mathbf{n_r}$ is a unit vector. In the limit $a \to 0$, with a being the lattice spacing, $\mathbf{r}$ becomes a continuous variable and $\mathbf{n_r}$ turns into a field $\mathbf{n}(\mathbf{r})$. The resulting classical magnetic energy is,

$$\mathcal{W} = \int d\mathbf{r}[\tilde{J}(\nabla\mathbf{n})^2 + \mathcal{E}_{\rm DM} - B_z n_z]\,, \tag{S11}$$

where $\mathcal{E}_{\rm DM}$ is the Dzyaloshinskii-Moriya (DM) interaction and it is equal to,

$$\mathcal{E}_{C_{2v}} = \mathcal{D}[\mathcal{L}^{(y)}_{yz} - \mathcal{L}^{(x)}_{xz}]\,, \quad \mathcal{E}_{D_{2d}} = -\mathcal{D}[\mathcal{L}^{(y)}_{xz} + \mathcal{L}^{(x)}_{yz}] \tag{S12}$$

$$\mathcal{E}_{\rm cub} = -\mathcal{D}[\mathcal{L}^{(y)}_{xz} + \mathcal{L}^{(x)}_{zy}]\,, \quad \mathcal{E}_{\rm int} = \mathcal{D}[\mathcal{L}^{(x)}_{zx} + \mathcal{L}^{(y)}_{zy}] \tag{S13}$$

for the C_{2v} symmetry, the D_{2d} symmetry, the cubic, and the interfacial DM interaction, respectively. The Lifshitz invariant is denoted as $\mathcal{L}^{(k)}_{ij} = n^i\partial^j_n/\partial^k_x - n^j\partial^i_n/\partial^k_x$. The parameters in (S11) are related to those in Eq. (1) from the main text via $\{\tilde{J}, \mathcal{D}, B_z\} = \{S^2J, S^2D/a, g\mu_{\rm B}SB/a^2\}$, and without loss of generality we assume $\mathcal{D} > 0$. Using the spherical parametrization $\mathbf{n} = [\sin\Theta\cos\Phi, \sin\Theta\sin\Phi, \cos\Theta]$, (anti)skyrmions appear as particle-like metastable solutions of the functional in Eq. (S11), described by $\Phi(\mathbf{r}) = -Q\phi + \gamma$ and the approximate function $\Theta(\rho) = 2\tan^{-1}[(\lambda_0/\rho)e^{-(\rho-\lambda_0)/\rho_0}]$, with $\mathbf{r} = (\rho, \phi)$ the polar coordinate system, γ the helicity, $\rho_0 = \sqrt{2\tilde{J}/B_z}$, while λ_0, which we obtain numerically from the

Euler-Lagrange equation of the stationary skyrmion, is the skyrmion radius.

Magnetic Excitations. Next we consider fluctuations around the static skyrmion as $\Phi = \Phi_0 + \xi = \mu\phi + \gamma + \xi$ and $\Theta = \Theta_0 + \eta$ and rewrite the energy functional as $\mathcal{W} = \mathcal{W}_0 + \chi^\dagger \mathcal{H} \chi$, where $\mathcal{W}_0(\Phi_0, \Theta_0)$ is the configuration energy functional of the (anti)skyrmion field, and $\mathcal{H}$ is the magnon Hamiltonian calculated for the convenient spinor representation $\chi = 1/2(\xi \sin\Theta_0 - i\eta, \xi \sin\Theta_0 + i\eta)^T$. Magnon states are found by solving the eigenvalue problem (EVP) $\mathcal{H}\Psi_n = \mathcal{E}_n \sigma_z \Psi_n$, while it appears convenient to represent these solutions in terms of wave expansions $\Psi_n = e^{im\phi}\psi_{n,m}(\rho)$. The EVP is written as $\mathcal{H}_m \psi_{n,m}(\rho) = \mathcal{E}_{n,m}\sigma_z \psi_{n,m}(\rho)$, with

$$\mathcal{H}_m = \tilde{J}(-\nabla_\rho^2 + U_0(\rho) + \frac{m^2}{\rho^2})\mathbb{1} + W(\rho)\sigma_x + \mu m V(\rho)\,, \tag{S14}$$

where $V(\rho)$, $W(\rho)$ and $U_0(\rho)$ are potentials of the radial coordinate ρ (for explicit expressions see Ref.,[6] and in particular Eqs. (D1)–(D3) therein). Solutions of the EVP include propagating scattering states with eigenfrequencies above the magnon gap $\varepsilon_{\rm gap} = g\mu_B B$, as well as massive internal modes that are found for energies $0 < \mathcal{E}_n \leq \varepsilon_{\rm gap}$ and correspond to deformations of the skyrmion into polygons. From the explicit form of $\mathcal{H}_m$ given in Eq. (S14), it becomes apparent that if $e^{im\phi}\psi_{n,m}(\rho)$ is a magnetic excitation over the skyrmionic field ($\mu = 1$), then $e^{-im\phi}\psi_{n,m}(\rho)$ is an excitation over the antiskyrmionic field ($\mu = -1$), with the same energy. These two states have an opposite sense of gyration, $\sim \cos(\mathcal{E}_{n,m}t \pm m\phi)$, respectively.

We now turn our attention to the calculation of the interaction potential $E_{\rm int}$, between the two topological particles. In the continuum limit, the bilayer interacting Hamiltonian equals $H_{\rm int} = -J_{\rm int}\int \mathbf{n}_1(\mathbf{r}) \cdot \mathbf{n}_2(\mathbf{r}) d\mathbf{r}$. Since the skyrmion is a localized object, we can get an intuition of the interlayer interaction by introducing a set of collective coordinates as $\mathbf{n}_i(\mathbf{r}) = \mathbf{n}_i(\mathbf{r} - \mathbf{R}_i)$, where here $\mathbf{R}_i$ represents the particle center of mass, and $i = 1, 2$ is the layer index. Thus, particles on different layers interact through a potential of the form

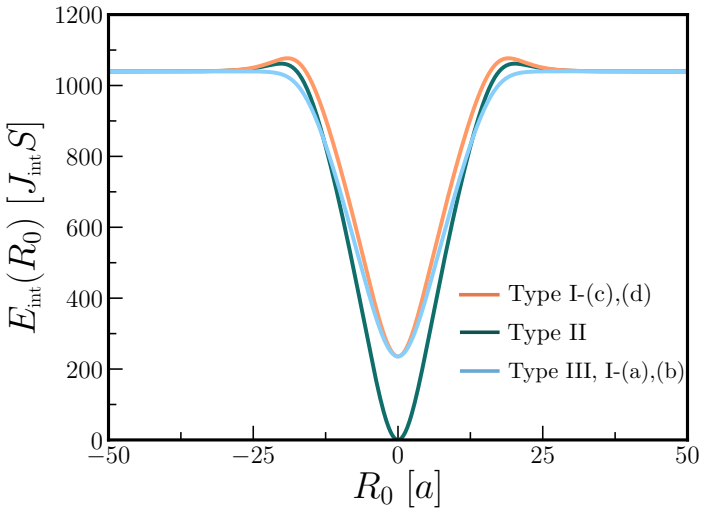

Figure S6: Interaction potential as a function of the distance of the center-of-mass of the two particles. Topological textures with different helicities have the same interaction energy, irrespective of their topological charge (blue line). Textures with the same helicity interact via a potential that distinguishes between pairs with the same (green line) or opposite topological charge (orange line). Each topological particle is of size $8.8a$.

$E_{\rm int}(R_0) = J_{\rm int} \int d\mathbf{r}[1-\mathbf{n}_1(\mathbf{r}-\mathbf{R}_1)\cdot\mathbf{n}_2(\mathbf{r}-\mathbf{R}_2)]$, and $R_0 = |\mathbf{R}_1-\mathbf{R}_2|$.[7] For reasons of simplicity, in all considered cases, the J and D couplings in both layers have the same strength, thus the skyrmion and antiskyrmion have the same size, which is determined by the competition among the Heisenberg, DM, and Zeeman interaction. The behavior of $E_{\rm int}$, depicted in Fig. S6, depends on both the helicity and the topological charge of the composite pair. Topological textures with different helicities have the same interaction energy, irrespective of their topological charge (blue line). Textures with the same helicity interact via a potential that distinguishes between pairs with the same (green line) or opposite topological charge (orange line).

As a final note, we derive the equation of motion for the collective coordinate of the topological charge separation for the Type I bilayer. Employing Thiele's approach[8] in the limit $Q \gg \alpha$, we obtain the equation of motion for the collective coordinates of position of

each layer $\mathbf{R}_i$,

$$-Q_i \epsilon_{\nu\mu} \dot{R}_i^\mu = \frac{\partial E_{\rm int}}{\partial R_i^\nu} + f_i^\nu(t)\,, \tag{S15}$$

where $i = 1, 2$ is the layer index, $\mu, \nu = x, y$, $\epsilon_{\mu\nu}$ is the antisymmetric tensor, $E_{\rm int}$ is the interaction energy due to the interlayer coupling, and $f_i^\nu(t)$ is a time-periodic function of frequency ω, which parametrizes the interaction between the coordinate R_i^ν and the gyrotropic mode activated by the in-plane time-periodic magnetic field. For the special case of the Type I bilayer, we note that Eq. (S15) is considerably simplified by making use of the fact that the two layers host particles with opposite topological charge, $Q_1 = -Q_2$, and the property $\partial E_{\rm int}/\partial R_1^\nu = -\partial E_{\rm int}/\partial R_2^\nu$. Thus, the equation of motion for $\mathbf{R}_0 = \mathbf{R}_1 - \mathbf{R}_2$ takes the form $-Q\epsilon_{\nu\mu}\dot{R}_0^\mu = f_0^\nu(t)$, with $Q = Q_1$. In view of the numerical results for $\mathbf{R}_0$, we use the ansatz $f_0^\nu(t) = F_\nu(\tilde{\gamma})\cos(\omega t)$, with $F_x(\tilde{\gamma}) = c\sin(\tilde{\gamma}/2)$, $F_y(\tilde{\gamma}) = c\cos(\tilde{\gamma}/2)$, and c a constant, allowing for a dependence on the helicity difference $\tilde{\gamma} = \gamma_1 - \gamma_2$.

References

(1) Dzyaloshinsky, I. A thermodynamic theory of "weak" ferromagnetism of antiferromagnetics. *Journal of Physics and Chemistry of Solids* **1958**, *4*, 241 – 255.

(2) Moriya, T. Anisotropic Superexchange Interaction and Weak Ferromagnetism. *Phys. Rev.* **1960**, *120*, 91–98.

(3) Tatara, G.; Kohno, H.; Shibata, J. Microscopic approach to current-driven domain wall dynamics. *Physics Reports* **2008**, *468*, 213 – 301.

(4) Oosterom, A. V.; Strackee, J. The Solid Angle of a Plane Triangle. *IEEE Trans. Biomed. Eng.* **1983**, *BME-30*, 125–126.

(5) Berg, B.; Lüscher, M. Definition and statistical distributions of a topological number in the lattice O(3) σ-model. *Nucl. Phys. B* **1981**, *190*, 412 – 424.

(6) Psaroudaki, C.; Aseev, P.; Loss, D. Quantum Brownian motion of a magnetic skyrmion. *Phys. Rev. B* **2019**, *100*, 134404.

(7) Koshibae, W.; Nagaosa, N. Theory of skyrmions in bilayer systems. *Scientific Reports* **2017**, *7*, 42645.

(8) Thiele, A. A. Steady-State Motion of Magnetic Domains. *Phys. Rev. Lett.* **1973**, *30*, 230–233.